



HAL
open science

In situ plasma and neutral gas observation time windows during a comet flyby: Application to the Comet Interceptor mission

J. de Keyser, N. J. T. Edberg, P. Henri, H. -U. Auster, M. Galand, M. Rubin, H. Nilsson, J. Soucek, N. André, V. Della Corte, et al.

► To cite this version:

J. de Keyser, N. J. T. Edberg, P. Henri, H. -U. Auster, M. Galand, et al.. In situ plasma and neutral gas observation time windows during a comet flyby: Application to the Comet Interceptor mission. *Planetary and Space Science*, 2024, 244, 10.1016/j.pss.2024.105878 . insu-04551236

HAL Id: insu-04551236

<https://insu.hal.science/insu-04551236>

Submitted on 18 Apr 2024

HAL is a multi-disciplinary open access archive for the deposit and dissemination of scientific research documents, whether they are published or not. The documents may come from teaching and research institutions in France or abroad, or from public or private research centers.

L'archive ouverte pluridisciplinaire **HAL**, est destinée au dépôt et à la diffusion de documents scientifiques de niveau recherche, publiés ou non, émanant des établissements d'enseignement et de recherche français ou étrangers, des laboratoires publics ou privés.



Distributed under a Creative Commons Attribution - NonCommercial 4.0 International License



Contents lists available at ScienceDirect

Planetary and Space Science

journal homepage: www.elsevier.com/locate/pss

In situ plasma and neutral gas observation time windows during a comet flyby: Application to the Comet Interceptor mission

J. De Keyser^{a,b,*}, N.J.T. Edberg^c, P. Henri^{d,e}, H.-U. Auster^f, M. Galand^g, M. Rubin^h, H. Nilssonⁱ, J. Soucek^j, N. André^k, V. Della Corte^l, H. Rothkaehl^m, R. Funaseⁿ, S. Kasahara^o, C. Corral Van Damme^p

^a Space Physics Division, Royal Belgian Institute for Space Aeronomy (BIRA-IASB), Ringlaan 3, B-1180, Brussels, Belgium

^b Center for mathematical Plasma Astrophysics, Katholieke Universiteit Leuven, Celestijnenlaan 200B, B-3001, Heverlee, Belgium

^c Swedish Institute of Space Physics (IRF), Uppsala, Sweden

^d Laboratoire de Physique et Chimie de l'Environnement et de l'Espace (LPC2E), CNRS, Orléans, France

^e Laboratoire Lagrange, Observatoire de la Côte d'Azur, Université Côte d'Azur (OCA), CNRS, Nice, France

^f Institut für Geophysik und Extraterrestrische Physik, Technische Universität Braunschweig, Braunschweig, Germany

^g Department of Physics, Imperial College London (ICL), London, UK

^h Space Research and Planetary Sciences, Physikalisches Institut, Universität Bern, Bern, Switzerland

ⁱ Swedish Institute of Space Physics (IRF), Kiruna, Sweden

^j Department of Space Physics, Institute of Atmospheric Physics CAS, Prague, Czech Republic

^k Institut de Recherche en Astrophysique et Planétologie, CNRS-UPS-CNES, Toulouse, France

^l INAF – Istituto di Astrofisica e Planetologia Spaziali (INAF-IAPS), Uppsala, Italy

^m CBK, Polish Academy of Sciences, Warsaw, Poland

ⁿ Japan Aerospace Exploration Agency, Institute of Space and Astronautical Science, Sagamihara, Japan

^o Department of Earth and Planetary Science, The University of Tokyo, Tokyo, Japan

^p European Space Agency, ESTEC, Noordwijk, The Netherlands

ARTICLE INFO

Dataset link: <http://dx.doi.org/10.18758/71021087>

Keywords:

Comet plasma

Comet bow shock

In situ plasma measurements

Multi-point measurements

Comet Interceptor

ABSTRACT

A comet flyby, like the one planned for ESA's Comet Interceptor mission, places stringent requirements on spacecraft resources. To plan the time line of in situ plasma and neutral gas observations during the flyby, the size of the comet magnetosphere and neutral coma must be estimated well. For given solar irradiance and solar wind conditions, comet composition, and neutral gas expansion speed, the size of gas coma and magnetosphere during the flyby can be estimated from the gas production rate and the flyby geometry. Combined with flyby velocity, the time spent in these regions can be inferred and a data acquisition plan can be elaborated for each instrument, compatible with the limited data storage capacity. The sizes of magnetosphere and gas coma are found from a statistical analysis based on the probability distributions of gas production rate, flyby velocity, and solar wind conditions. The size of the magnetosphere as measured by bow shock standoff distance is 10^5 – 10^6 km near 1 au in the unlikely case of a Halley-type target comet, down to a nonexistent bow shock for targets with low activity. This translates into durations up to 10^3 – 10^4 seconds. These estimates can be narrowed down when a target is identified far from the Sun, and even more so as its activity can be predicted more reliably closer to the Sun. Plasma and neutral gas instruments on the Comet Interceptor main spacecraft can monitor the entire flyby by using an adaptive data acquisition strategy in the context of a record-and-playback scenario. For probes released from the main spacecraft, the inter-satellite communication link limits the data return. For a slow flyby of an active comet, the probes may not yet be released during the inbound bow shock crossing.

1. Introduction

Comet exploration with a flyby mission was pioneered by the spacecraft flotilla sent to 1P/Halley, with Giotto passing at 600 km distance

from the nucleus, and Vega 1 and 2, Suisei, and Sakigake farther out (Reinhard, 1986). In 1992 Giotto flew by 26P/Grigg-Skjellerup at 200 km distance (Morley, 1991; McDonnell et al., 1993). Other comet

* Corresponding author at: Space Physics Division, Royal Belgian Institute for Space Aeronomy (BIRA-IASB), Ringlaan 3, B-1180, Brussels, Belgium.
E-mail address: Johan.DeKeyser@aeronomie.be (J. De Keyser).

<https://doi.org/10.1016/j.pss.2024.105878>

Received 20 December 2023; Received in revised form 5 March 2024; Accepted 7 March 2024

Available online 11 March 2024

0032-0633/© 2024 The Author(s). Published by Elsevier Ltd. This is an open access article under the CC BY-NC license (<http://creativecommons.org/licenses/by-nc/4.0/>).

flybys that provided plasma and field data included Deep Space 1 at 19P/Borrelly (Boice et al., 2000) and ICE (ISEE-3) at 21P/Giacobini–Zinner (Brandt et al., 1985). ESA’s Rosetta mission was not a flyby mission but accompanied 67P/Churyumov–Gerasimenko for a large fraction of its orbit, staying close to the nucleus for detailed monitoring of the surface and to study gas coma composition (10–200 km, except when performing excursions). This constrained the exploration of the comet’s plasma environment and its interaction with the interplanetary medium. Also, 67P represents the case of a relatively low-activity comet (Goetz et al., 2022).

Comet Interceptor (CI), an F-class mission in the ESA Science Programme to be launched in 2029, will attempt to flyby a long-period comet, ideally a dynamically new one (Jones et al., 2024; Snodgrass and Jones, 2019). One of the scientific objectives is multi-point in situ observation of the comet environment (Jones et al., 2022). The main spacecraft (S/C A) plans to make upstream in situ and remote sensing observations of the target from afar, to protect it from the dust environment. Two small probes (S/C B1 provided by JAXA, B2 by ESA) will venture closer to the target and carry complementary instruments to build up a 3D picture of the comet, using S/C A as communications hub with Earth. Such multi-point measurements are possible, for instance, with the three magnetometers on A, B1 and B2.

CI will wait around L2 until a target is identified. The design of a trajectory to intercept the target faces many uncertainties but is necessary to estimate ΔV and to foresee the corresponding amount of propellant (Sanchez et al., 2021). The present paper focuses on uncertainties related to the flyby itself. It tries to assess the duration of the time windows when in situ plasma and neutral gas instruments can expect relevant measurements. Such estimates must necessarily be parameterized by the flyby geometry and comet characteristics. The motivation is two-fold.

1. First, the estimated time windows must be combined with an observation plan specifying which instrument modes are used when, in order to verify that the consumed power remains compatible with the spacecraft resources during the flyby. Since the flyby dictates spacecraft attitude (for camera pointing and keeping the dust shield in the ram direction), direct data transmission to Earth is not possible. Because of this, but also because the data acquisition rate is much larger than the transmission rate, the scientific instruments are operated in a record-and-playback mode. The observation plan therefore must respect the on-board data storage limits.
2. Second, S/C A performs maneuvers in the run-up to closest approach (CA), including the release of the probes and telecommunications sessions, all of which require attitude changes and/or thruster firings. These may interfere with the operation of some of the instruments (e.g., by changing the thermal environment or by requiring high voltages to be off during thruster operations). Ideally, such maneuvers should not interfere with any time-critical measurements.

While this paper addresses the Comet Interceptor mission and in particular the Dust, Fields, and Plasma sensors (DFP) on S/C A and B2 and the Plasma Suite (PS) on B1, as well as the neutral gas MANiaC sensors on S/C A (Jones et al., 2022), the methodology and the results have broader relevance.

2. Methods

Fig. 1 sketches the typical flyby geometry. The nucleus is the source of an expanding cloud of neutral gas (yellow) that becomes ionized (red) by various mechanisms, including photo-ionization. The densest part of the cometary plasma is referred to as the ionosphere. Ionized cometary molecules are picked up by the interplanetary magnetic field, thus slowing down the solar wind (blue), a process known as mass-loading. As the solar wind is supersonic and super-Alfvénic, a

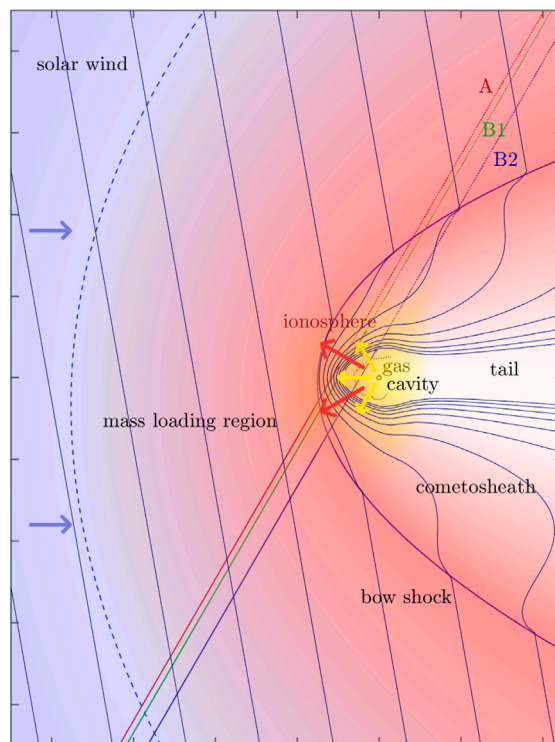


Fig. 1. Sketch of the structure of a comet magnetosphere and a typical Comet Interceptor flyby geometry. The Sun is to the left. This figure presents a projection onto the ecliptic plane, while the three S/C trajectories will not all lie in the same plane. (Size of nucleus and diamagnetic cavity exaggerated).

bow shock forms upstream of the ionosphere. The shocked solar wind interacts with the cometary plasma and forms a diamagnetic cavity, which acts as an obstacle in the flow. Magnetic field lines are draped around the comet ionosphere, enveloping the diamagnetic cavity as the region from which the field is excluded by currents in the diamagnetic cavity boundary. This section introduces the models used to assess at any time during the flyby whether meaningful plasma and neutral gas observations can be conducted.

2.1. Parameters

Comet activity can be described in terms of the gas and dust production rates Q_{gas} and Q_{dust} , and (volatile) composition. The flyby geometry is specified by the cometocentric distance R_{CA} of the spacecraft at closest approach (in what follows this is applied to S/C A), the relative flyby velocity vector $\mathbf{v}_{\text{flyby}}$, the heliocentric distance r_{flyby} of the comet at the time of the flyby, and other orbital parameters. Environmental parameters that affect the flyby include solar wind density n_{sw} , velocity \mathbf{u}_{sw} , and interplanetary magnetic field \mathbf{B}_{sw} . All parameters are summarized in Table 1.

Since the CI target might not be known even at the time of launch, most of these parameters remain unknown at present (Snodgrass and Jones, 2019). To facilitate planning, the CI team has defined plausible target and flyby parameter values to guide the design of the instruments, of the spacecraft, and of the mission (Pinzan et al., 2023). The present study statistically examines a range of parameter values around these typical ones to assess how the uncertainty affects the observation time line.

The flyby will take place in or near the ecliptic plane, at a heliocentric distance r_{flyby} between 0.9 and 1.2 au (Snodgrass and Jones, 2019). Statistical studies (Jones et al., 2022) show that the flyby velocity is between 10 and 70 km s⁻¹, with a most probable value of 50 km s⁻¹; the spacecraft must be designed to withstand dust particle

Table 1
Physical quantities (with value if fixed).

Quantity	Symbol	Units
<i>General</i>		
Cometocentric distance	R	km
Heliocentric distance	r	au
Boltzmann constant	k_B	$1.38 \times 10^{-23} \text{ J K}^{-1}$
<i>Solar wind properties</i>		
Solar wind density	n_{sw}	m^{-3}
Solar wind velocity	\mathbf{u}_{sw}	km s^{-1}
Interplanetary magnetic field	\mathbf{B}_{sw}	nT
Solar wind ion mass	m_{sw}	1 Da
Solar wind ion temperature	T_{swi}	K
Solar wind electron temperature	T_{swe}	K
Solar wind plasma beta	β_{sw}	
Solar wind magnetic pressure	$P_{sw,mag}$	Pa
Solar wind kinetic pressure	$P_{sw,kin}$	Pa
<i>Comet properties</i>		
Radius of the nucleus	$R_{nucleus}$	2.5 km
Neutral gas production rate	Q_{gas}	molecules s^{-1}
Dust production rate	Q_{dust}	kg s^{-1}
Neutral gas density	n_n	m^{-3}
Neutral gas expansion speed	u_n	1 km s^{-1}
Cometary ion mass	m_i	19 Da
Distribution of Q_{gas} (1 au)	f_{random}	per bin
Biased distribution of Q_{gas} (1 au)	f_{biased}	per bin
<i>Bow shock physics and ion pickup</i>		
Ionization rate	ν	s^{-1}
Bow shock position	R_{BS}	km
Mass-loading region limit	R_{ML}	km
Bow shock stand-off distance	$R_{BS,K}$	km
Auxiliary parameter	A	
Terminator bow shock position	$(R_{BS,K}, f_{flank})$	km
Critical normalized mass flux	$(\rho u_x)_{crit}^*$	4/3
Ion travel distance to full pickup	R_s	km
Ion gyrofrequency	Ω_{ci}	rad s^{-1}
Ion pickup time	t_p	s
Gyration angle before pickup	$\Omega_{ci} t_p$	$2\pi \cdot 0.216 \text{ rad}$
Shape model parameter	ϵ	1
Mass-loading limit relative to shock	γ	5
<i>Flyby properties</i>		
Heliocentric distance of the flyby	r_{flyby}	au
Closest approach distance	R_{CA}	km
Zenith angle at closest approach	θ_{CA}	30°
Relative flyby velocity	\mathbf{v}_{flyby}	km s^{-1}
Neutral gas density detection limit	n_n^*	m^{-3}
Neutral gas detection distance	R_n	km
In/outbound bow shock position	R_{BS1}, R_{BS2}	km
In/outbound mass-loading limit	R_{ML1}, R_{ML2}	km
Time from CA to R_n	t_n	s
Time from CA to R_{BS1}, R_{BS2}	t_{BS1}, t_{BS2}	s
Time from CA to R_{ML1}, R_{ML2}	t_{ML1}, t_{ML2}	s
<i>COMPLIMENT data storage</i>		
Total memory available	M	3000 Mbit
Total data recording time	T	s
Fractions spent in each mode	a, b, c	$\in [0, 1]$
Housekeeping data rate	ρ_{HK}	128 bps
Low resolution science data rate	ρ_{low}	327 bps
Reduced science data rate	ρ_{red}	9792 bps
Full science data rate	ρ_{full}	33 435 bps

impacts at these speeds. At 1 au and near the ecliptic plane, solar wind density is $0.1\text{--}10$ particles cm^{-3} , while solar wind velocity can be $350\text{--}800 \text{ km s}^{-1}$, although a speed around 400 km s^{-1} is most probable, depending on solar activity. The gas production rate Q_{gas} (1 au) can range from around 10^{28} molecules s^{-1} (exemplified by 67P with a peak water production of 4×10^{28} molecules s^{-1} at 1.24 au (Hansen et al., 2016)) or lower, up to 10^{30} molecules s^{-1} (as for 1P with $Q_{gas} = 6.9 \times 10^{29}$ molecules s^{-1} at 0.89 au (Krankowsky et al., 1986)) or even up to $10^{31} \text{--}10^{32}$ molecules s^{-1} (C/1995 O1 Hale-Bopp with $Q_{gas} = 3.59 \times 10^{31}$ molecules s^{-1} around perihelion at 0.91 au (Bair et al.,

2018)). The odds to be able to target a comet with a high production rate during the mission timeframe are very slim (see Section 3.2). Some of the backup targets have very low activity, e.g., $Q_{dust}/Q_{dust,1P}$ is 7×10^{-5} for 15P/Finlay, 2×10^{-7} for 289P/Blanpain, and 8×10^{-6} for 300P/Catalina (Kidger, 2023). Assuming $Q_{dust}/Q_{dust,1P} = Q_{gas}/Q_{gas,1P}$, their gas production rate is $<10^{26}$ molecules s^{-1} .

2.2. Plasma and neutral gas observation windows

We examine the duration of the time periods around CA during which S/C A is able to perform in situ measurements of plasma phenomena and of the neutral gas. We distinguish the periods during which continuous observation is recommended in order not to miss any crucial parts of the comet environment (e.g., the bow shock crossings) and those where observations are possible but not necessarily needed. Both time periods have direct implications on the planning of the spacecraft and instrument operations, the data volume that can be acquired, the sensor integration times to be used, etc. Pinzan et al. (2023).

The study is conceived as a series of estimates of the locations and times when different phenomena can be observed, with an emphasis on those that take place relatively far away from the nucleus, since they set the bounds of the observation windows.

2.3. Neutral gas coma

The neutral gas emanating from the comet nucleus expands as it flows out into space (see Fig. 1). As the coma density n_n decreases with cometocentric distance, there is a critical distance R_n beyond which the density is below the detection limit n_n^* of the neutral gas sensors.

For the CI/MANiAC Neutral Density Gauge (NDG) a lower pressure bound of 10^{-11} mbar is given (Jones et al., 2022). Assuming thermalization in the antechamber to a temperature of 300 K, this corresponds to a density $n_n^* = 10^5$ molecules cm^{-3} , while the Rosetta/ROSINA COMetary Pressure Sensor (COPS) measured gas density down to 10^6 molecules cm^{-3} (Balsiger et al., 2007; Schläppi et al., 2010). The CI/MANiAC time-of-flight (TOF) mass spectrometer aims at a sensitivity that is 100 times better at $n_n^* = 10^3$ molecules cm^{-3} (Jones et al., 2022).

A difficulty will be the spacecraft background created by diffusion, desorption, and material decomposition. On Rosetta, the S/C background dropped to a pressure level of 10^{-10} to 10^{-11} mbar after a few years in space (Schläppi et al., 2010), i.e., 10^5 molecules cm^{-3} . Rosetta/ROSINA COPS was still capable of measuring this. During the high-relative-velocity CI flyby, an additional background contribution can be expected from neutrals sputtered from the spacecraft surface by hypervelocity dust particle impacts. The CI/MANiAC time-of-flight mass spectrometer should be able to characterize this background before and after the flyby as it typically is only present for selected species. As long as it behaves in a predictable manner so that it can be modeled, the background can be subtracted away.

For an isotropic and spherically expanding neutral coma, the neutral density is $n_n = Q_{gas}/(4\pi u_n R^2)$ with R the cometocentric distance and u_n the neutral gas expansion speed. A typical value is $u_n = 1 \text{ km s}^{-1}$, which can approximately be taken constant although there might be a weak dependence on Q_{gas} . In the absence of an extended source of grains containing ices, and for as long as the amount of ionization is negligible, the neutral gas detection limit is reached at

$$R_n = \sqrt{\frac{Q_{gas}}{4\pi u_n n_n^*}} \quad (1)$$

The CI/MANiAC NDG should be able to detect the gas coma out to $R_n = 3000$, 30 000, and 3×10^5 km for $Q_{gas} = 10^{28}$, 10^{30} , and 10^{32} molecules s^{-1} , respectively. For the CI/MANiAC TOF spectrometer, $R_n = 3 \times 10^4$, 3×10^5 , and 3×10^6 km, respectively.

If only the nucleus' day side is outgassing, R_n is a factor $\sqrt{2}$ larger. If there are localized outgassing enhancements by a factor of 10, the distances are a factor $\sqrt{10}$ larger. In a collision-dominated

coma, such local density enhancements diffuse laterally and tend to disappear with cometocentric distance. At any point in a collisionless coma, gas originating from different spots on the illuminated surface is superposed, so that localized density enhancements tend to average out. Nevertheless, diurnal variations in outgassing by an order of magnitude are very well possible, especially with a non-convex nucleus, as observed near 67P (e.g., Hansen et al., 2016), but keeping in mind that diurnal variations may be hard to identify during a flyby if its duration is much shorter than the nucleus rotation period. For studies of coma composition, the detection limit should be compared to the partial densities of the relevant gas components rather than the total density, so that n_n should be at least one order of magnitude larger than n_n^* , especially if one is interested in minor species and a decent signal-to-noise ratio.

In conclusion, the neutral gas can be detected from considerable distances from the nucleus, up to 10^6 km for very active comets, although the larger end of the range may be overestimated as photoionization and dissociative photoionization processes can no longer be neglected for such long distances. Combining a neutral outflow $u_n = 1$ km s⁻¹ with a photo-dissociation and photo-ionization time scale $1/\nu$ (1 au) close to 10^6 s, the maximum size of the gas coma can approach 10^6 km. The detectable gas coma of low-activity comets is significantly smaller. For studies of minor gas coma constituents, the relevant R_n are correspondingly smaller. The signal-to-noise ratio is highest near CA as the gas density peaks there. Practical limitations are set by spacecraft outgassing, so that a good background characterization is needed. Outgassing therefore is a key driver of the design of CI/MANiAC and of the spacecraft near the instrument. Starting observations early, continuing them regularly throughout the flyby, and ending them only after exiting from the gas coma, is useful both for assessing changes in the gas production and for monitoring the evolving spacecraft background.

2.4. Comet bow shock

The neutral gas originating from the nucleus becomes ionized through various mechanisms. This ultimately creates the comet magnetosphere. An important outer boundary of the magnetosphere is the bow shock (see Fig. 1). The model of Koenders et al. (2013) gives the bow shock standoff distance as

$$R_{BS,K} = \frac{\nu Q_{gas} m_i}{4\pi u_n m_{sw} n_{sw} u_{sw} [(\rho u_x)_{crit}^* - 1 + A]} - R_s, \quad (2)$$

in which ν is the net ionization rate. The (average) cometary ion mass is taken to be $m_i = 19$ Da corresponding to H_3O^+ , because photoionization in a H_2O -dominated coma gives rise to H_2O^+ , which in turn may undergo a proton transfer in reaction with water, leading to H_3O^+ . Typically H_3O^+ dominates at low cometocentric distances, while H_2O^+ dominates farther out (Beth et al., 2019). The solar wind is taken to consist of protons only, so $m_{sw} = 1$ Da. The dimensionless quantity $(\rho u_x)_{crit}^* = 4/3$ is the critical normalized mass flux density required for the solar wind to slow down enough to form a shock (Biermann et al., 1967; Koenders et al., 2013; Edberg et al., 2023). R_s is the distance an ion travels before being accelerated to solar wind speed,

$$R_s = \frac{u_{sw}}{\Omega_{ci} [\Omega_{ci} t_p - \sin(\Omega_{ci} t_p)]} \quad (3)$$

with $\Omega_{ci} = eB/m_i$ in rad s⁻¹ the ion gyrofrequency of singly charged ions in magnetic field B and t_p the pick-up time in seconds. A value $\Omega_{ci} t_p = 2\pi 0.216$ rad is typical (Koenders et al., 2013). The dimensionless quantity

$$A = \frac{\nu Q_{gas} m_i}{4\pi u_n n_{sw} m_{sw} u_{sw} (u_n/\nu + R_{nucleus})} \quad (4)$$

(where $R_{nucleus}$ is the radius of the nucleus, taken here to be 2.5 km) limits the standoff distance for high gas production to

$$R_{BS,K} \leq u_n/\nu. \quad (5)$$

We have evaluated Koenders' model for heliocentric distances 0.9 au, 1.0 au, and 1.2 au, the range accessible by CI (Jones et al., 2022, 2024). Q_{gas} is taken to scale with heliocentric distance as

$$Q_{gas}(r_{flyby}) = \frac{Q_{gas}(1 \text{ au})}{r_{flyby}^6} \quad (6)$$

where the exponent is the average of the inbound and outbound variation seen at 67P (Hansen et al., 2016). The ionization rate is assumed to follow an inverse square law with heliocentric distance so that

$$\nu(r_{flyby}) = \frac{\nu(1 \text{ au})}{r_{flyby}^2}, \quad (7)$$

with r_{flyby} in au and $\nu(1 \text{ au}) = 7 \times 10^{-7}$ s⁻¹ the ionization rate in a water-dominated coma at 1 au, corresponding to the average solar activity from the Rosetta era (Vigren et al., 2019; Edberg et al., 2023); this value fits in the range given by Huebner and Mukherjee (2015). We do not consider here the variability of the EUV flux with solar activity (which can be up to an order of magnitude). The above scaling assumes that photoionization dominates and that the coma is not opaque. A loss of opacity occurs for high activity in the inner coma and quenches the comet's activity (Beth et al., 2019). While in principle valid only for low activity, the model of Koenders and this scaling of ν still hold approximately for more active comets. Typical solar wind speed is $u_{sw} = 400$ km s⁻¹. At 1 au, representative values of solar wind density $n_{sw} = 11$ particles cm⁻³ and magnetic field strength $B_{sw} = 7.6$ nT are considered, leading to $\Omega_{ci} = 0.0386$ rad s⁻¹, $t_p = 35.1$ s, $R_s = 3900$ km. Solar wind density and magnetic field strength scale with $1/r_{flyby}^2$ and $1/r_{flyby}^{1.348}$, while solar wind velocity does not change (Khabarova and Obridko, 2012). The results are shown in Fig. 2 for $Q_{gas}(1 \text{ au})$ varying from 10^{28} to 10^{32} molecules s⁻¹. The panels show the neutral gas detection limit R_n corresponding to $n_n^* = 10^5$ and 10^3 molecules cm⁻³ for the MANiAC NDG and TOF spectrometer (see Section 2.3, dashed red lines) that varies with Q_{gas} as a power law (slope 1/2), the bow shock standoff distance $R_{BS,K}$ for the parameters given above (solid blue line), and the bow shock distance at the terminator following the shape model explained below (dashed green line). The bow shock standoff distance levels off for high Q_{gas} to $u_n/\nu = 1.4 \times 10^6$ km at 1 au (from Eq. (5)) so that $R_{BS,K}$ does not change much for $Q_{gas}(1 \text{ au}) > 10^{31}$ molecules cm⁻³. No bow shock exists at 1.2 au for $Q_{gas}(1 \text{ au}) < 2 \times 10^{28}$ molecules s⁻¹ as outgassing is too weak there (gray shaded area). From Rosetta at 67P it is known that a "bow wave" or "infant bow shock" may exist in this situation, rather than a fully developed bow shock (Gunell et al., 2018).

A shape model is required to make predictions about where S/C A will cross the bow shock. A model that is often used for planetary bow shocks is of the form

$$R_{BS} = \frac{1 + \epsilon}{1 + \epsilon \cos \theta} R_{BS,K}, \quad (8)$$

where θ is the angle relative to the solar wind ram direction (there generally is a small aberration angle with respect to the sun-comet line) and where $\epsilon > 0$ is a dimensionless free parameter. The position of the bow shock at $\theta = 90^\circ$ is then

$$R_{BS,K,flank} = (1 + \epsilon) R_{BS,K}. \quad (9)$$

A trajectory passing close to the nucleus, with $R_{CA} \ll R_{BS,K}$, oriented at an arbitrary angle, will cross the bow shock at a distance below $R_{BS,K,flank}$ during the inbound leg and above it during the outbound leg, or the reverse, with a total distance traveled inside the bow shock $> 2(1 + \epsilon) R_{BS,K}$. The dashed green line in Fig. 2 represents $R_{BS,K,flank}$ for $\epsilon = 1$. This value has been established by Edberg et al. (2023). They have examined a collection of observed bow shock crossings from the literature. Using the shape model, the corresponding standoff distances have been inferred. Furthermore, they have used published results of comet simulations to obtain the standoff distances directly. The resulting set of bow shock standoff distances combines data for different

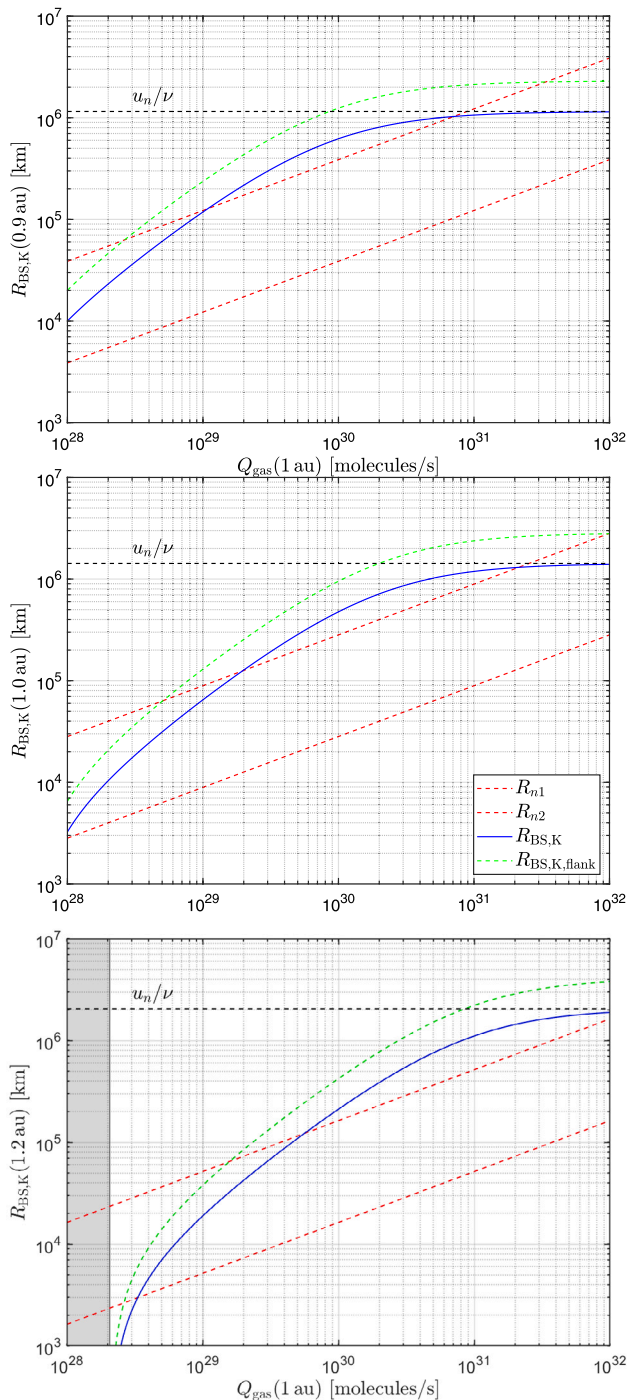


Fig. 2. Bow shock standoff distance $R_{BS,K}$ as a function of Q_{gas} (1 au) (solid blue line), bow shock distance at terminator (green), and neutral gas detection limits for MANiaC NDG and TOF (red). The horizontal black line gives the maximum $R_{BS,K}$ possible. When outgassing is too weak, a proper bow shock may not exist (shaded area).

ionization rates and different solar wind conditions, corresponding to different heliocentric distances, all inside 3 au. When plotted as a function of Q_{gas} , the bow shock standoff distances compared well to the model of Koenders with parameters typical for 1 au, for Q_{gas} ranging from 10^{27} to 10^{32} molecules s^{-1} .

It can be concluded that the position of the bow shock is well described by the model of Koenders combined with a simple shape model. Nevertheless, predicting the bow shock position remains difficult:

- If Q_{gas} is known up to an order of magnitude, the uncertainty in $R_{BS,K}$ is also an order of magnitude, except for very active comets where $R_{BS,K}$ is close to the upper limit of Eq. (5).
- The gas production rate may vary due to diurnal or seasonal effects, and the spatial distribution of the gas may be nonuniform due to nucleus geometry (Hansen et al., 2016). As CI flies by the comet, it detects gas released from different positions at different times corresponding to different nucleus spin phases.
- Solar wind properties and solar EUV flux fluctuate all the time.
- The shape of the magnetosphere can be asymmetric due to aberration effects and due to the anisotropy introduced by the interplanetary magnetic field (Nilsson et al., 2021).

All of this results in an uncertainty on the bow shock standoff distance that is hard to eliminate in advance, so that it is difficult to adjust the operations planning to it. One therefore must continuously measure the plasma so as not to miss the bow shock crossings, especially since the bow shock has been identified as an important CI science topic (Jones et al., 2022, 2024).

2.5. Unperturbed solar wind, mass loading, pick-up ions and associated plasma waves

The solar wind–comet interaction starts well in front of the bow shock. Neutrals become ionized and these ions are picked-up by the solar wind, resulting in a solar wind deceleration as the energy for pick-up ion acceleration is drawn from the solar wind kinetic energy (see Fig. 1). The ion particle distributions change as a consequence of pickup (Coates, 2004). As indicated by Edberg et al. (2023), pick-up ions have been observed more than an order of magnitude farther out than the bow shock. Unperturbed solar wind measurements must be acquired to assess the solar wind forcing of the comet magnetosphere. By performing solar wind measurements before entering into and after exiting from the mass-loading region, these can be matched up to solar wind models to estimate the actual conditions during the flyby, which is important since no upstream solar wind measurements are available while the S/C are near CA.

The ion pick-up process upstream of the bow shock, and the associated solar wind deceleration, have not yet been studied very well at comets, with information mostly from Giotto’s Halley and Grigg–Skjellerup flybys. The CI/DFP-SCIENA ion spectrometer could make a valuable contribution on this topic. Because of the lack of detailed information, it is simply assumed here that the mass-loading region is within

$$R_{ML} = \gamma R_{BS}, \quad (10)$$

where $\gamma = 5$ reflects how far this region extends out into the solar wind, although we do not know the exact shape of that region. Hybrid simulations show pick-up to occur out to such distances (e.g. Delamere, 2006; Simon Wedlund et al., 2017). In conclusion, mass loading starts at a distance that is an order of magnitude larger than the bow shock position. While scientifically interesting, continuous measurements in this region are not mandatory.

3. Statistics of observation window duration

To deal with the difficulty of predicting where and for how long the comet’s neutral gas and plasma environment can be sampled, a statistical analysis has been carried out. The analysis examines the situation for a range of hypothetical comets, flyby properties, and solar wind conditions to find the probability distribution of the observation window durations.

3.1. Analysis for given r_{flyby} and Q_{gas}

In a first step, the comet properties are considered given, with a fixed value of Q_{gas} and with the v , u_n , m_i , $\Omega_{ci}t_p$, R_{nucleus} , and ϵ values introduced earlier (see Table 1).

The comet flyby trajectory is assumed to be within the ecliptic plane at a given heliocentric distance r_{flyby} , with a closest approach of S/C A at $R_{\text{CA}} = 1000$ km. This currently is the nominal distance but it can be fine-tuned somewhat shortly before the flyby as a function of the comet gas and dust production rates. Closest approach is taken to occur at a solar zenith angle $\theta_{\text{CA}} = 30^\circ$ in the pre-noon sector, the configuration shown in Fig. 1. This leads to inbound and outbound bow shock crossings at R_{BS1} and R_{BS2} , respectively, that are characterized by $R_{\text{BS,K}} < R_{\text{BS1}} < 2R_{\text{BS,K}} < R_{\text{BS2}}$. If closest approach occurs on the dayside with θ_{CA} close to zero, then $R_{\text{BS,K}} \leq R_{\text{BS1}} \approx R_{\text{BS2}} < 2R_{\text{BS,K}}$. If closest approach occurs at larger solar zenith angle, R_{BS2} can become significantly larger than $2R_{\text{BS,K}}$. A similar reasoning applies to R_{ML} , with the caution that not much is known about the actual shape of the mass loading region. In our statistical analysis, the geometry is kept fixed in order to simplify the problem, but also because $R_{\text{BS,K}}$ dictates the scale size of the plasma observation window regardless of the specifics of the flyby geometry.

A parameter that is of major importance is the flyby velocity. We consider v_{flyby} to follow a β distribution defined over the domain $[10, 70]$ km s $^{-1}$ with $\alpha = 6$ and $\beta = 4$, which is asymmetric with a maximum around 50 km s $^{-1}$, i.e., a distribution of the form

$$f(v_{\text{flyby}}) \propto x^{\alpha-1}(1-x)^{\beta-1}$$

where $x = (v_{\text{flyby}} [\text{km s}^{-1}] - 10)/60$; this distribution represents the observational data in Jones et al. (2024, Figure 37).

Solar wind speed is randomly chosen between slow (normal distribution centered around 400 km s $^{-1}$ with standard deviation 30 km s $^{-1}$) and fast (normal distribution centered around 650 km s $^{-1}$ with standard deviation 50 km s $^{-1}$), with slow wind 3 times more likely than fast wind (McComas et al., 2000). Plasma temperature at 1 au is taken to change with speed, with $T_{\text{swi}}(1 \text{ au}) = 700(u_{\text{sw}} [\text{km s}^{-1}] - 200) \text{ K}$ and $T_{\text{swe}}(1 \text{ au}) = T_{\text{swi}}/5$ (Elliott et al., 2012). Magnetic pressure $P_{\text{sw,mag}}(1 \text{ au})$ is taken from a normal distribution centered around the pressure corresponding to a reference magnetic field of 7.6 nT, with a 5% standard deviation. From this, the magnetic field $B_{\text{sw}}(1 \text{ au})$ is computed and scaled to $B_{\text{sw}}(r_{\text{flyby}})$ (Khabarova and Obridko, 2012). Solar wind plasma beta is taken from a lognormal distribution: $\log_{10}(\beta_{\text{sw}}(1 \text{ au}))$ has a normal distribution around -0.2 with a standard deviation 0.5 (Mullan and Smith, 2006). Then the kinetic pressure at 1 au is found from

$$P_{\text{sw,kin}}(1 \text{ au}) = \beta(1 \text{ au})P_{\text{sw,mag}}(1 \text{ au}) \quad (11)$$

and hence solar wind density is computed from

$$n_{\text{sw}}(1 \text{ au}) = P_{\text{sw,kin}}(1 \text{ au})/k_B[T_{\text{swi}}(1 \text{ au}) + T_{\text{swe}}(1 \text{ au})], \quad (12)$$

which is then scaled to obtain $n_{\text{sw}}(r_{\text{flyby}})$. These choices provide representative solar wind characteristics.

Fig. 3 shows the results for comet flybys at 1 au. The top half of the figure gives the probability distributions for the relevant positions, while the bottom half displays the distributions of the corresponding times from closest approach. The calculation is performed for $Q_{\text{gas}} = 10^{28}$ (red curves), 10^{30} (green) and 10^{32} molecules s $^{-1}$ (blue).

The neutral gas detection limit is at a fixed R_n regardless of the solar wind conditions, because it only depends on Q_{gas} and u_n ; solid and dashed lines correspond to the 10^5 cm^{-3} and the 10^3 cm^{-3} limits for the CI/MANiAc NDG and TOF sensors. R_n scales with $\sqrt{Q_{\text{gas}}}$. For a comet with low activity, neutral measurements are relevant essentially within a few thousand kilometers, while for an extremely active one the gas coma can be detected up to 10^6 km, comparable to the scale length of loss of neutral H $_2$ O molecules due to photoionization. The corresponding times t_n are identical for the inbound and outbound

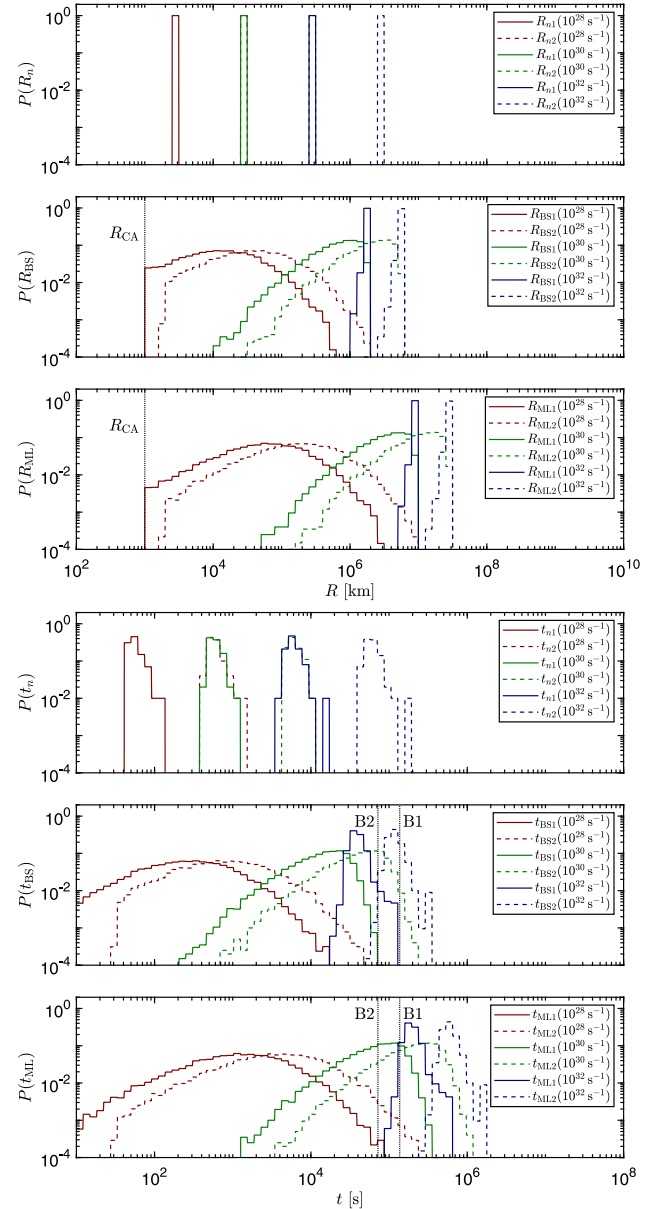


Fig. 3. Probability distributions of relevant distances and times for flybys at 1 au, for comets with $Q_{\text{gas}}(1 \text{ au}) = 10^{28}$, 10^{30} , and 10^{32} molecules s $^{-1}$ (red, green, blue, respectively). The spatial extent of the neutral gas detection region R_n is set by activity; R_{n1} and R_{n2} reflect the detection limits for the CI/MANiAc NDG and TOF spectrometer, respectively. The corresponding times t_{n1} and t_{n2} show a spread due to the unknown v_{flyby} . The distributions of the in- and outbound bow shock crossing positions, R_{BS1} and R_{BS2} , are broad but can never be inward of R_{CA} . The distributions of the corresponding times, t_{BS1} and t_{BS2} , show an even larger spread due to v_{flyby} . Note that the inbound bow shock crossing may occur before the release of probe B1 and/or B2. The distributions of entry into and exit from the mass-loading region, R_{ML1} and R_{ML2} , and the corresponding times, t_{ML1} and t_{ML2} , are broader by the factor γ .

leg of the flyby. Their values show a spread according to the v_{flyby} variability. For low comet activity and high flyby speed, the time suitable for neutral measurements is only a few minutes, while for extreme activity and low flyby speed, the period extends over many hours. For $Q_{\text{gas}} = 10^{30}$ molecules s $^{-1}$, measurements are possible within 10^4 s (3 h) around CA for a 50 km s $^{-1}$ flyby. For smaller comas, t_n depends on R_{CA} .

A large spread is observed in the bow shock crossing positions due to the varying solar wind properties. The distribution of R_{BS} is sharply truncated at R_{CA} at its lower edge for low activity comets, because the

Table 2

Typical extent and duration of the observation windows for $Q_{\text{gas}} = 10^{30}$ molecules s^{-1} and $v_{\text{flyby}} = 50$ km s^{-1} .

	r_{flyby}		
	0.9 au	1.0 au	1.2 au
Neutral observations			
$2t_n$ (limit 10^5 cm^{-3})	1.6×10^3 s	1.2×10^3 s	0.6×10^3 s
$2R_n$ (limit 10^5 cm^{-3})	8×10^4 km	6×10^4 km	3×10^4 km
$2t_n$ (limit 10^3 cm^{-3})	1.6×10^4 s	1.2×10^4 s	0.6×10^4 s
$2R_n$ (limit 10^3 cm^{-3})	8×10^5 km	6×10^5 km	3×10^5 km
Plasma observations — continuous			
$t_{\text{BS1}} + t_{\text{BS2}}$	10×10^4 s	8×10^4 s	4×10^4 s
$R_{\text{BS1}} + R_{\text{BS2}}$	5×10^6 km	4×10^6 km	2×10^6 km
Plasma observations — desired			
$t_{\text{ML1}} + t_{\text{ML2}}$	5×10^5 s	4×10^5 s	2×10^5 s
$R_{\text{ML1}} + R_{\text{ML2}}$	2.5×10^7 km	2×10^7 km	1×10^7 km

bow shock is not traversed when $R_{\text{BS}} < R_{\text{CA}}$, so that $t_{\text{BS}} = 0$. Bow shock crossing distances may be up to 10^6 km even in the low activity case. The corresponding time duration inside the bow shock can reach 10^4 s, i.e., several hours. For $Q_{\text{gas}} = 10^{30}$ molecules s^{-1} , the bow shock is at a few times 10^6 km and the duration up to 10^5 s, about a day, for a 50 km s^{-1} flyby. For the extreme activity situation, the bow shock crossings are situated around almost 10^7 km. The corresponding time interval of interest is several times 10^5 s, i.e., several days, but this situation is very unlikely. With the approximation adopted here it is clear that the distances R_{ML} and relevant times t_{ML} are up to $5 \times$ larger than R_{BS} and t_{BS} .

A similar analysis has been conducted for flybys at 1.2 au and 0.9 au (Figs. 4 and 5). Using the scaling of Eq. (6), the gas production at $r_{\text{flyby}} = 1.2 \text{ au}$ is reduced by a factor of 3 compared to 1 au. From the model of Koenders, it is expected that the bow shock position scales as

$$R_{\text{BS}} \propto \frac{v Q_{\text{gas}}}{n_{\text{sw}}} \propto \frac{(1/r_{\text{flyby}}^2)(1/r_{\text{flyby}}^6)}{1/r_{\text{flyby}}^2} = \frac{1}{r_{\text{flyby}}^6}, \quad (13)$$

at least when A and R_c can be ignored. R_{BS} thus decreases farther from the Sun, which leads to shorter observation durations. Conversely, at 0.9 au the gas production is enhanced by a factor of 1.9 and thus the comet magnetosphere is larger. For very high activity, however, the model of Koenders limits the standoff distance to u_n/v , so that $R_{\text{BS}} \propto r_{\text{flyby}}^2$. The physical interpretation is that photoionization is lower farther away from the Sun and thus the bow shock forms farther out. This counteracts the effect of the lower gas production rate farther from the Sun. As a result, the size does not change much with r_{flyby} for large Q_{gas} .

Table 2 presents the results for $Q_{\text{gas}} = 10^{30}$ molecules s^{-1} at 1 au, somewhat higher than the 1P/Halley-like activity that CI originally set out to be able to deal with. The most likely science observation windows for neutral measurements ($2t_n$) and for plasma measurements ($t_{\text{BS1}} + t_{\text{BS2}}$ and $t_{\text{ML1}} + t_{\text{ML2}}$) are listed, corresponding essentially to the 50 km s^{-1} flyby speed, but should be considered with care. There is a spread on the results due to solar wind variability and uncertain flyby speed. The comet activity Q_{gas} itself varies in space and time. The neutral gas expansion speed was considered constant, while in reality it varies somewhat with Q_{gas} . The observation window for neutral measurements depends on a successful spacecraft background correction. For plasma measurements, the model of Koenders has its limits, especially at low Q_{gas} where a bow shock even may not exist and at high Q_{gas} where additional ionization mechanisms should be accounted for. Despite all these caveats, the order of magnitude should be correct. For a 10^{30} molecules s^{-1} comet, the most likely science observation window is $3\text{--}5 \times 10^5$ s, i.e., 4 to 6 days, not necessarily centered around the time of closest approach, with considerable spread. Continuous observations are needed for $0.6\text{--}1 \times 10^5$ s, i.e., 16 to 27 h.

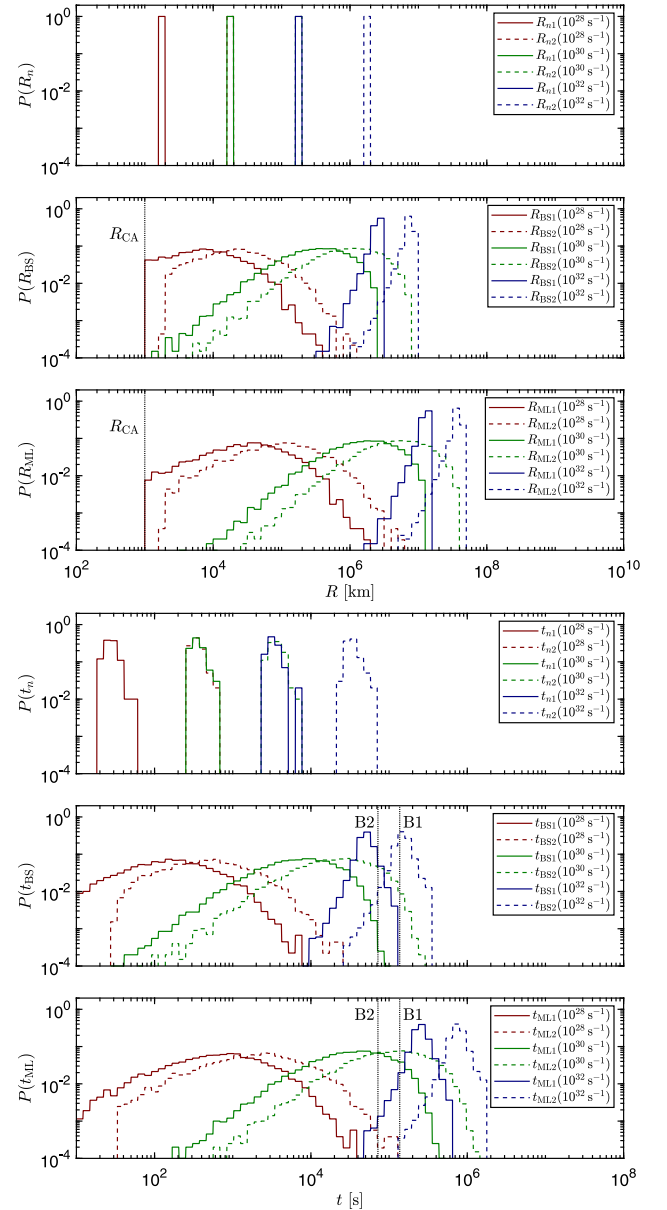


Fig. 4. Probability distributions of relevant distances and times for flybys at 1.2 au; layout identical as for Fig. 3.

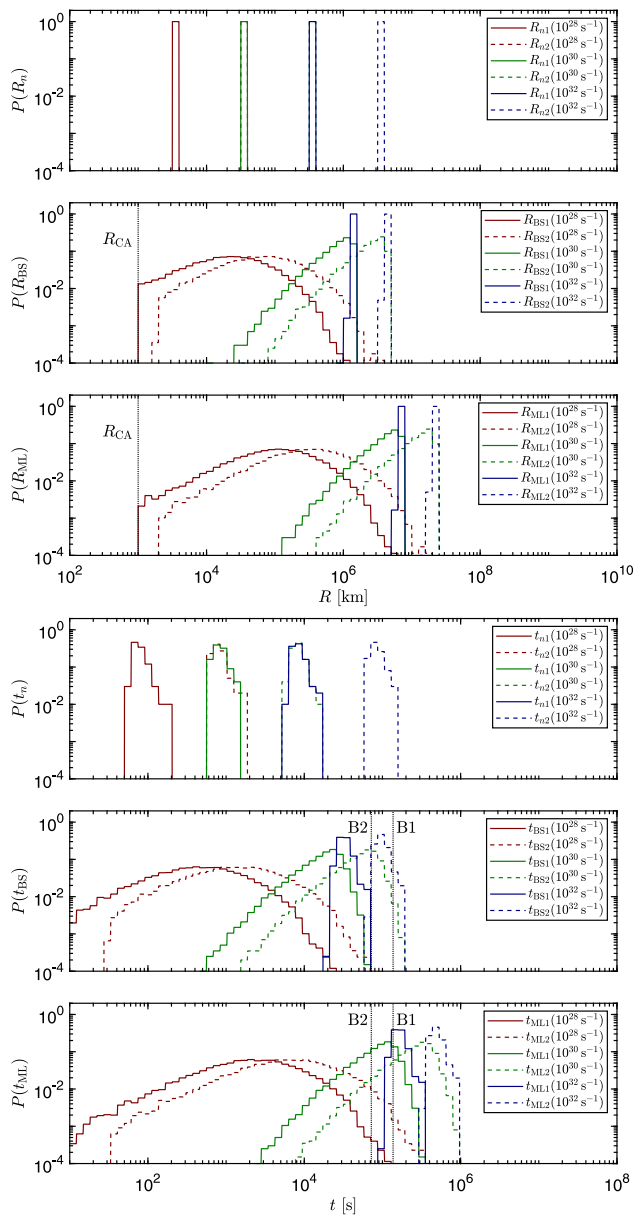


Fig. 5. Probability distributions of relevant distances and times for flybys at 0.9 au; layout identical as for Fig. 3.

3.2. Analysis for given r_{flyby} and target selection bias

The observation window strongly depends on comet activity. Therefore, as a next step, the expected comet activity distribution is incorporated in the statistical analysis. Kidger (2023, Table 2) gives the recurrence frequency of comets as a function of their peak dust activity relative to 1P. These numbers are obtained from the 173 “new” comets observed between 1880 and 1978, which have a perihelion inside 1.2 au. In what follows, it is assumed that this peak activity does not differ much from the activity at 1 au, at least in a statistical sense.

To obtain the activity statistics for the CI target, however, besides the statistics of the comets as they occur in nature, one needs to take into account also selection effects related to the discovery of potential targets. The CI project plans to exploit the observations of the Vera C. Rubin survey telescope, formerly known as the LSST, Ivezić et al. (2019) to detect comets when they are still far away from the Sun, so that the spacecraft has enough time to cruise towards the interception point (Snodgrass and Jones, 2019). Discovering faraway comets

adds potential targets but also leads to an observational bias towards larger and higher albedo objects. Another selection effect comes from accessibility considerations: It is not because the comet orbit has a perihelion inside 1.2 au that its ecliptic crossings occur in the 0.9–1.2 au range. Mission operations constraints create an additional bias. For instance, the flyby preferably should not take place when the comet is too close to the Sun’s direction as seen from Earth, which could hamper radio communication. The statistics of CI targets also depend on the decision logic of the CI team. Will the project go for the first comet that is discovered and that fits the technical constraints? Will the project choose the most active comet among the potential candidates, because this facilitates neutral gas composition studies or because it offers a fluid-scale magnetosphere as opposed to the kinetic-scale magnetosphere of 67P? Or will the team avoid too active comets because of the dust impact risks? Some of these topics have been already addressed by Vigen et al. (2023). The statistical results for two strategies are presented below.

The first strategy is to pick a target comet randomly among the candidates, with the only requirement that the mass production rate is above $Q_{\text{gas}} = 10^{28}$ at 1 au. This is assuming that the discovery selection effect is negligible for comet nuclei with such activity levels, and that the accessibility and technical constraints do not introduce a bias. Above this lower activity limit, the risk of too low neutral gas densities and/or of not even crossing the bow shock is virtually zero. The corresponding distribution $f_{\text{random}}(Q_{\text{gas}}(1 \text{ au}))$ is shown as the red histogram in Fig. 6. This distribution is obtained from the recurrence frequencies of Kidger (2023), extrapolated towards lower and higher activity using power laws, constrained to the interval $[10^{28}, 10^{32}]$ molecules s^{-1} , and normalized (see also Table 3). While Kidger (2023) gives the distribution in terms of dust activity relative to 1P, we translate this into gas production rate relative to 1P, with a reference value $Q_{\text{gas},1\text{P}}(1 \text{ au}) = 3.4 \times 10^{29}$ molecules s^{-1} (scaled from the Krankowsky et al. (1986) value using Eq. (6)) in the assumption that gas and dust production rates scale proportionally. Lower-activity objects clearly dominate the distribution. The odds for a target with $Q_{\text{gas}}(1 \text{ au}) > 10^{29}$ molecules s^{-1} are only 3%; the odds that it has $Q_{\text{gas}}(1 \text{ au}) > 10^{30}$ molecules s^{-1} are practically zero. Following Kidger (2023), one can expect about 2 comets with $Q_{\text{gas}} > 0.05 Q_{\text{gas},1\text{P}}(1 \text{ au}) \approx 2 \times 10^{28}$ molecules s^{-1} during a 6-year mission like that of Comet Interceptor. Performing the statistical analysis for R_n , R_{BS} , R_{ML} and for t_n , t_{BS} , t_{ML} , for a sample where $Q_{\text{gas}}(1 \text{ au})$ follows the f_{random} distribution, results in the red curves shown in Fig. 7 for $r_{\text{flyby}} = 1.0$ au. Not surprisingly, these distributions are broad and only slightly shifted upward from those obtained for $Q_{\text{gas}}(1 \text{ au}) = 10^{28}$ molecules s^{-1} .

The second strategy considers a modest observational or target selection bias towards higher Q_{gas} , which is more realistic. This distribution is obtained as

$$f_{\text{biased}}(Q_{\text{gas}}(1 \text{ au})) \propto Q_{\text{gas}}(1 \text{ au}) f_{\text{random}}(Q_{\text{gas}}(1 \text{ au})), \quad (14)$$

the green histogram in Fig. 6, where the maximum of the distribution is very broad and centered around 10^{29} molecules s^{-1} . The odds for a target with Q_{gas} below or above 10^{29} are 79% and 21%, respectively; the situation $Q_{\text{gas}} > 10^{30}$ molecules s^{-1} occurs in about 0.2% of the cases. It is therefore logical that the overall distributions shown in green in Fig. 7 are broad, covering ranges between those for 10^{28} and 10^{30} molecules s^{-1} . Adding such a further selection bias reduces the number of potential targets even further; one simply may not have the luxury to do so.

4. Implications for data acquisition

The analysis of neutral gas and plasma observation windows has shown that an observation time of 10^5 s (continuous observation + selected observation periods in the solar wind and mass loading regions) is not unlikely. This has implications for the onboard data storage,

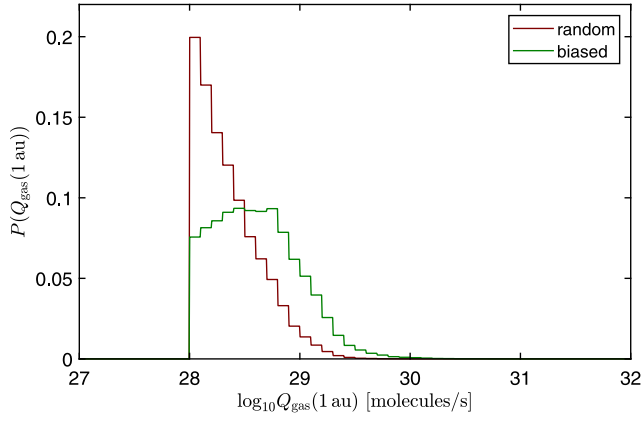


Fig. 6. Distribution of Q_{gas} (1 au) for the random (red) and biased (green) target selection scenarios. See main text for more explanations.

Table 3

Random and biased comet activity distributions.

$\log_{10} Q_{\text{gas}}$ (1 au) [molecules s ⁻¹]	f_{random} [per bin]	f_{biased} [per bin]
28.0–28.1	0.1996	0.0756
28.1–28.2	0.1700	0.0814
28.2–28.3	0.1404	0.0857
28.3–28.4	0.1203	0.0910
28.4–28.5	0.0985	0.0935
28.5–28.6	0.0759	0.0921
28.6–28.7	0.0621	0.0916
28.7–28.8	0.0493	0.0933
28.8–28.9	0.0331	0.0786
28.9–29.0	0.0203	0.0618
29.0–29.1	0.0137	0.0513
29.1–29.2	0.0086	0.0397
29.2–29.3	0.0046	0.0257
29.3–29.4	0.0020	0.0146
29.4–29.5	0.0009	0.0084
29.5–29.6	0.0004	0.0055
29.6–29.7	0.0003	0.0035
29.7–29.8	0.0001	0.0024
29.8–29.9	0.0001	0.0014
29.9–30.0	0.0000	0.0010
30.0–30.1	0.0000	0.0008
30.1–30.2	0.0000	0.0005
30.2–30.3	0.0000	0.0003
30.3–30.4	0.0000	0.0002
30.4–30.5	0.0000	0.0001
30.5–30.6	0.0000	0.0001
30.6–30.7	0.0000	0.0001
30.7–30.8	0.0000	0.0000

given that S/C A will record all data during the flyby for later transmission to ground. Data storage is examined here for the Langmuir probe and Mutual Impedance experiment CI/DFP-COMPLIMENT, part of the Dust-Fields-Plasma instrument (Jones et al., 2022, section 4.1.4.3), but the other plasma sensors face a comparable situation.

The COMPLIMENT data must be stored locally in the 8 Gbyte flash memory of the DFP-A Dust and Plasma Processing Unit (Soucek and Kolmasova, 2023). The exact partitioning of that memory among the DFP-A sensors has not yet been decided. Let M be the storage available to COMPLIMENT during the flyby, with data acquisition rates (Rothkaehl et al., 2022a,b):

- housekeeping rate $\rho_{\text{HK}} = 128$ bps
- low resolution science rate $\rho_{\text{low}} = 327$ bps
- reduced science rate $\rho_{\text{red}} = 9792$ bps
- full science rate $\rho_{\text{full}} = 33435$ bps

The instrument operation is identical for the low, reduced science, and full science modes; they only differ in how much of the data is kept

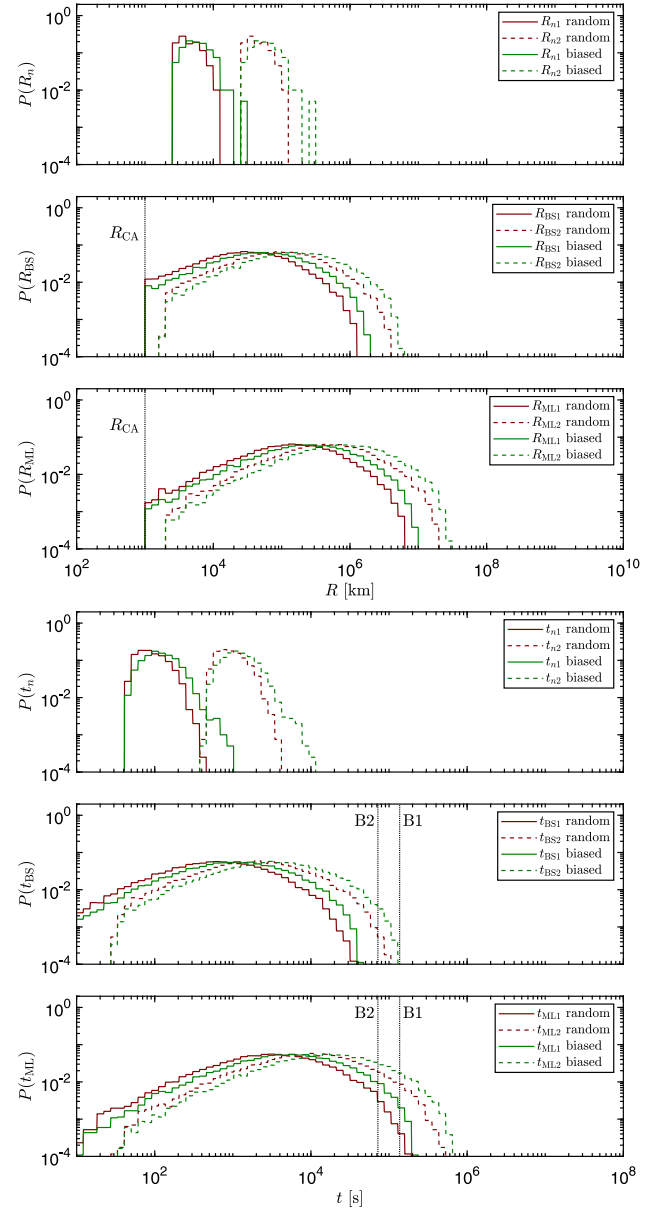


Fig. 7. Probability distributions of relevant distances and times for flybys at 1 au, for comets with Q_{gas} (1 au) following the f_{random} (red) and f_{biased} (green) statistics. The spatial characteristics R_{n1} , R_{n2} , $R_{\text{BS}1}$, $R_{\text{BS}2}$, $R_{\text{ML}1}$ and $R_{\text{ML}2}$, as well as the corresponding times t_{n1} , t_{n2} , $t_{\text{BS}1}$, $t_{\text{BS}2}$, $t_{\text{ML}1}$ and $t_{\text{ML}2}$, tend to be somewhat larger for the biased scenario which features higher activity on average.

in memory. There is no data compression prior to storage. A margin of 20% is applied to the above data acquisition rates for packetization and overhead.

If the total observation time is T , the average science data rate is

$$\langle \rho \rangle = (M - T\rho_{\text{HK}})/T, \quad (15)$$

where the numerator represents the amount of memory available for science data. One then has

$$a\rho_{\text{low}} + b\rho_{\text{red}} + c\rho_{\text{full}} = \langle \rho \rangle, \quad \text{with } a + b + c = 1, \quad (16)$$

where a , b , c are the time fractions spent in each of the science modes. For a given ratio c/b , and defining the quantity

$$\rho^* = \frac{\rho_{\text{red}} + \rho_{\text{full}}c/b}{1 + c/b}, \quad (17)$$

Table 4
Data storage strategies for COMPLIMENT for a range of science observation window durations.

T [s]	$c/b = 0.1$			$c/b = 0.5$			$c/b = 1.0$		
	a	b	c	a	b	c	a	b	c
10 000	0.00	0.00	1.00	0.00	0.00	1.00	0.00	0.00	1.00
20 000	0.00	0.00	1.00	0.00	0.00	1.00	0.00	0.00	1.00
50 000	0.00	0.00	1.00	0.00	0.00	1.00	0.00	0.00	1.00
100 000	0.00	0.00	1.00	0.00	0.00	1.00	0.00	0.00	1.00
200 000	0.00	0.00	1.00	0.00	0.00	1.00	0.00	0.00	1.00
500 000	0.00	0.83	0.17	0.22	0.52	0.26	0.36	0.32	0.32
1 000 000	0.44	0.51	0.05	0.62	0.25	0.13	0.70	0.15	0.15
5 000 000	0.92	0.07	0.01	0.94	0.04	0.02	0.96	0.02	0.02
10 000 000	0.98	0.02	0.00	0.99	0.01	0.00	0.98	0.01	0.01

one finds

$$a = \frac{\rho^* - \langle \rho \rangle}{\rho^* - \rho_{\text{low}}}, \quad b = \frac{1 - a}{1 + c/b}, \quad c = 1 - a - b, \quad (18)$$

so that the recorded data amounts to the available memory M . If $a < 0$, there is sufficient memory so that low resolution is not needed. One then sets $a = 0$ and computes

$$b = \frac{\rho_{\text{full}} - \langle \rho \rangle}{\rho_{\text{full}} - \rho_{\text{red}}}, \quad c = 1 - b, \quad (19)$$

where c/b is bigger than the originally specified one. If in this situation $b < 0$ (or, equivalently, $c > 1$), M is large enough to store all full science data.

This procedure has been employed to compute the optimum memory usage strategies in Table 4 with $M = 1$ Gbyte = 8000 Mbit and three different values of c/b . As can be seen from the table, all data can be recorded at full resolution for $T \leq 200\,000$ s. Above $T = 10^6$ s, only a few percent of the total science data can be recorded at full resolution. For long-duration flybys, an acceptable compromise for the scientists would be to work with a lower time resolution. Since the smaller scales are to be found in the densest plasma, near closest approach, it makes sense to plan the reduced and full science mode periods around closest approach or, if a limited degree of on-board processing is possible, to select a posteriori which data have to be stored at high time resolution and which do not. For $T > 10^7$ s, it is no longer possible to store all data.

For the B1 and B2 probes, memory size may not be the limitation, but the capacity of the inter-satellite link. The link capacity decreases with time as the probe separation increases. For probe B2, in addition, there is its limited lifetime that constrains which measurements can be acquired and transmitted.

5. Conclusions

Comet Interceptor is an ambitious mission in many respects. Since little is known about the potential target comets and flyby conditions, it must prepare for a broad range of possible situations and expect late modifications up to the beginning of the flyby. For S/C A, the observation window durations range up to 10^6 s, with continuous observations recommended up to 10^5 s, or even more in the unlikely case of a very active target, a slow flyby speed, and/or slow solar wind conditions. For the probes B1 and B2 the durations are slightly longer as they are closer to the nucleus (though this duration may be limited by their time of release from S/C A and by their lifetime). For high activity, the probes may even not have been released yet at the time of the bow shock crossings. For very low activity comets, including most of the backup targets, no bow shock forms and there might be little of a magnetosphere to study. Such a situation would also be very restrictive for neutral gas coma science.

At this point, it is not possible to accurately predict when scientific key events such as interesting plasma boundary crossings (there are more than the bow shock) will occur. It therefore appears highly desirable to plan for the plasma and field sensors on S/C A to remain in science acquisition mode during the entire flyby (including

slews, communication sessions, thruster firings and other spacecraft manoeuvres) over a time interval of 10^5 s around closest approach, to be sure to cover these key events, as long as this is compatible with mission and spacecraft constraints. As an example, the COMPLIMENT sensor can deal with an extended time window within the current memory allocation, simply by playing with the relative proportions of the low resolution, reduced, and full science modes; similar strategies can be adopted by the other sensors. It is more acceptable to be in a reduced science mode for a longer time, than to be OFF completely during shorter periods. For some sensors, it might be advantageous to switch to lower resolution during spacecraft slews and communications sessions, if the changing attitude would degrade the quality of the observations. Keeping some sensors ON (or in STANDBY) also helps to ensure thermal stability and thus facilitates data calibration. The instruments on probes B1 and B2 are operated based on power and inter-satellite link considerations.

Planning for a long observation duration on S/C A does not exclude adapting when more precise information becomes available. Once a target comet is identified, the heliocentric distance of the flyby, flyby speed and geometry can be determined, which helps to retire much of the uncertainty. Based on these quantities, the simulations can be repeated, still with unknown solar wind conditions and the uncertainty on Q_{gas} , since it may be hard to predict the gas production rate at the time of the flyby when the comet is still far away from the Sun. Closer to the actual flyby, an even better assessment is possible. A well-informed decision can then be made concerning the scheduling of the different operational modes of the in situ instruments, thereby optimizing the science return of the multi-point Comet Interceptor mission.

To a certain extent, the flyby geometry is scalable: for higher Q_{gas} , the flyby distance can be increased somewhat. However, there are limitations to that, as the time of release of the probes is fixed (B1 38 h before CA, B2 20 h before CA). This is because of the limited range of the inter-satellite communications link, as well as the finite lifetime of B2 battery power. A particular consequence is that, if the comet is very active, the spacecraft will see the inbound bow shock before probe release and the probes may already be out of communication range during the outbound bow shock pass, so that multi-point observations of the bow shock, e.g., with the three magnetometers, are out of reach.

CRedit authorship contribution statement

J. De Keyser: Writing – review & editing, Writing – original draft, Visualization, Validation, Supervision, Software, Resources, Project administration, Methodology, Investigation, Funding acquisition, Formal analysis, Conceptualization. **N.J.T. Edberg:** Writing – review & editing, Validation, Methodology, Conceptualization. **P. Henri:** Writing – review & editing, Validation. **H.-U. Auster:** Writing – review & editing. **M. Galand:** Writing – review & editing, Validation. **M. Rubin:** Writing – review & editing, Validation. **H. Nilsson:** Writing – review & editing. **J. Soucek:** Writing – review & editing. **N. André:** Writing – review & editing. **V. Della Corte:** Writing – review & editing. **H. Rothkaehl:** Writing – review & editing. **R. Funase:** Writing – review & editing. **S. Kasahara:** Writing – review & editing. **C. Corral Van Damme:** Writing – review & editing, Validation, Project administration.

Declaration of competing interest

The authors declare that they have no known competing financial interests or personal relationships that could have appeared to influence the work reported in this paper.

Data availability

The software used for this work is publicly available from <http://dx.doi.org/10.18758/71021087>.

Acknowledgments

Work by JDK has been supported by the Belgian Science Policy Office through ESA PRODEX PEA 4000139830. NE was supported by SNSA grant 2021-00047. Work by MR was funded by the Canton of Bern and the Swiss National Science Foundation (SNSF; 200020 207312). Work by MG was funded by the UK Space Agency (UKSA) under grant ST/X002349/1 and by the European Space Agency (ESA) under contract 4000130837/20/NL/IB/ig. French co-authors acknowledge the support of CNES to the Comet Interceptor mission. The authors acknowledge the feedback from the Comet Interceptor Science Operations Working Group.

References

- Bair, A.N., et al., 2018. The extremely active comet c/hale-bopp (1995 O1): Production rates from nearly five years of narrowband photometry. In: AAS/Division for Planetary Sciences Meeting Abstracts #50. In: AAS/Division for Planetary Sciences Meeting Abstracts, vol. 50, p. 210.06.
- Balsiger, H., et al., 2007. Rosina - rosetta orbiter spectrometer for ion and neutral analysis. Space Sci. Rev. 128 (1–4), 745–801. <http://dx.doi.org/10.1007/s11214-006-8335-3>.
- Beth, A., et al., 2019. Comparative study of photo-produced ionosphere in the close environment of comets. Astron. Astrophys. 630, A47. <http://dx.doi.org/10.1051/0004-6361/201833517>.
- Biermann, L., et al., 1967. The interactions of the solar wind with a comet. Sol. Phys. 1 (2), 254–284. <http://dx.doi.org/10.1007/BF00150860>.
- Boice, D.C., et al., 2000. The deep space 1 encounter with comet 19p/borrelly. Earth Moon Planets 89, 301–324. <http://dx.doi.org/10.1023/A:1021519124588>.
- Brandt, J.C., et al., 1985. The international cometary explorer (ICE) mission to comet giacobini-zinner (G/Z). In: Carusi, A., Valsecchi, G.B. (Eds.), Dynamics of Comets: Their Origin and Evolution. Springer Netherlands, Dordrecht, pp. 405–414. http://dx.doi.org/10.1007/978-94-009-5400-7_35.
- Coates, A.J., 2004. Ion pickup at comets. Adv. Space Res. 33 (11), 1977–1988. <http://dx.doi.org/10.1016/j.asr.2003.06.029>.
- Delamere, P.A., 2006. Hybrid code simulations of the solar wind interaction with Comet 19P/Borrelly. J. Geophys. Res. 111 (A12217), <http://dx.doi.org/10.1029/2006JA011859>.
- Edberg, N.J.T., et al., 2023. Scale size of cometary bow shocks. Astron. Astrophys. <http://dx.doi.org/10.1051/0004-6361/202346566>.
- Elliott, H.A., et al., 2012. Temporal and radial variation of the solar wind temperature-speed relationship. J. Geophys. Res. 117, A09102. <http://dx.doi.org/10.1029/2011JA017125>.
- Goetz, C., et al., 2022. The plasma environment of comet 67p/Churyumov-Gerasimenko. Space Sci. Rev. 216, 65. <http://dx.doi.org/10.1007/s11214-022-00931-1>.
- Gunell, H., et al., 2018. The infant bow shock: a new frontier at a weak activity comet. Astron. Astrophys. 619, L2. <http://dx.doi.org/10.1051/0004-6361/201834225>.
- Hansen, K.C., et al., 2016. Evolution of water production of 67p/Churyumov-Gerasimenko: An empirical model and a multi-instrument study. Mon. Not. R. Astron. Soc. 462, S491–S506. <http://dx.doi.org/10.1093/mnras/stw2413>.
- Huebner, W.F., Mukherjee, J., 2015. Photoionization and photodissociation rates in solar and blackbody radiation fields. Planet. Space Sci. 106, 11–45. <http://dx.doi.org/10.1016/j.pss.2014.11.022>.
- Ivezić, Ž., et al., 2019. LSST: From science drivers to reference design and anticipated data products. Astrophys. J. 873 (2), 111. <http://dx.doi.org/10.3847/1538-4357/ab042c>.
- Jones, G., Snodgrass, C., Tubiana, C., et al., 2024. The comet interceptor mission. Space Sci. Rev. 220 (9), <http://dx.doi.org/10.1007/s11214-023-01035-0>.
- Jones, G., et al., 2022. Comet interceptor: Visiting a pristine comet (red book).
- Khabarova, O., Obridko, V., 2012. Puzzles of the interplanetary magnetic field in the inner heliosphere. Astrophys. J. 761 (2), 82. <http://dx.doi.org/10.1088/0004-637X/761/2/82>.
- Kidger, M., 2023. Comet interceptor: A note on target selection in relation to the reference mission scenario, version 1.0.
- Koenders, C., et al., 2013. Revisiting cometary bow shock positions. Planet. Space Sci. 87, 85–95. <http://dx.doi.org/10.1016/j.pss.2013.08.009>.
- Krankowsky, D., et al., 1986. In situ gas and ion measurements at comet Halley. Nature 321 (Suppl 6067), 326–329. <http://dx.doi.org/10.1038/321326a0>.
- McComas, D.J., et al., 2000. Solar wind observations over Ulysses' first full polar orbit. J. Geophys. Res. 105 (A5), 10419–10433. <http://dx.doi.org/10.1029/1999JA000383>.
- McDonnell, J.A.M., et al., 1993. Dust particle impacts during the Giotto encounter with comet Grigg-Skjellerup. Nature 362, 732–734. <http://dx.doi.org/10.1038/362732a0>.
- Morley, T., 1991. The Giotto encounter with comet p/Grigg-Skjellerup. Eur. Space Agency Spec. Publ. ESA SP-326, 87–491.
- Mullan, D.J., Smith, C.W., 2006. Solar wind statistics at 1 au: Alfvén speed and plasma beta. Sol. Phys. 234, 325–338. <http://dx.doi.org/10.1007/s11207-006-2077-y>.
- Nilsson, H., et al., 2021. Birth of a magnetosphere. In: Magnetospheres in the Solar System. Wiley, pp. 427–439. <http://dx.doi.org/10.1002/9781119815624.ch27>, (Chapter 27).
- Pinzan, G., et al., 2023. Comet interceptor reference operations timeline for final approach and encounter, version 1.0.
- Reinhard, R., 1986. The Giotto encounter with comet Halley. Nature 321, 313–318. <http://dx.doi.org/10.1038/321313a0>.
- Rothkaehl, H., et al., 2022a. DFP-a instrument budgets, version 1.4.
- Rothkaehl, H., et al., 2022b. DFP-a instrument operations reference plan, version 1.6.
- Sanchez, J.P., et al., 2021. ESA F-class comet interceptor: Trajectory design to intercept a yet-to-be-discovered comet. Acta Astronaut. 188, 265–277. <http://dx.doi.org/10.1016/j.actaastro.2021.07.014>.
- Schläppi, B., et al., 2010. The influence of spacecraft outgassing on the exploration of tenuous atmospheres with in situ mass spectrometry. J. Geophys. Res. 115, A12313. <http://dx.doi.org/10.1029/2010JA015734>.
- Simon Wedlund, C., Alho, M., Gronoff, G., et al., 2017. Hybrid modelling of cometary plasma environments. I. Impact of photoionisation, charge exchange, and electron ionisation on bow shock and cometopause at 67p/Churyumov-Gerasimenko. Astron. Astrophys. 604 (A73), <http://dx.doi.org/10.1051/0004-6361/201730514>.
- Snodgrass, C., Jones, G.H., 2019. The European space agency's comet interceptor lies in wait. Nature Comm. 10, 5418. <http://dx.doi.org/10.1038/s41467-019-13470-1>.
- Soucek, J., Kolmasova, I., 2023. Dust and plasma processing unit (DAPU) application software user manual, version 0.2.
- Vigren, E., et al., 2019. The evolution of the electron number density in the coma of comet 67p at the location of rosetta from 2015 november through 2016 march. Astrophys. J. 881 (6), <http://dx.doi.org/10.3847/1538-4357/ab29f7>.
- Vigren, E., et al., 2023. A potential aid in the target selection for the comet interceptor mission. Planet. Space Sci. 237, 105765. <http://dx.doi.org/10.1016/j.pss.2023.105765>.